

INVITED ARTICLE

Dynamics of charge transfer at Au/Si metal-semiconductor nano-interface

Yulun Han^a, Sergei Tretiak^b and Dmitri Kilin^{a,*}

^aDepartment of Chemistry, University of South Dakota, Vermillion, USA; ^bLos Alamos National Laboratory, Center for Integrated Nanotechnology, Los Alamos, USA

(Received 15 May 2013; accepted 3 September 2013)

An *ab initio* analysis of the periodic array of Au/Si nanostructure composed of gold clusters linked to silicon quantum dot (QD) co-doped by aluminium and phosphorus along [111] direction is presented in this paper. The density functional theory (DFT) is used to compute the electronic structure of the simulated system. Non-adiabatic coupling implemented in the form of dissipative equation of motion for reduced density matrix is used to study the phonon-induced relaxation in the simulated system. The density of states clearly shows that the formation of Au–Si bonds contributes states to the band gap of the model. Dynamics of selected photo-excitations shows that hole relaxation in energy and in space is much faster than electron relaxation, which is due to the higher density of states of the valence band.

Keywords: silicon-gold contact; nanowires hot carrier relaxation; hybrid materials; non-adiabatic dynamics; p-n junction

1. Introduction

Silicon nanostructures have attracted intensive attention due to their extraordinary properties, such as excellent electronic/optical/mechanical properties [1], and can be used in various areas ranging from solar cells in photovoltaic industry [2] to biological sensing of DNA and proteins in biology [3]. To fully make use of these Si nanostructures, doping is of great importance [4]. A p–n junction, which is a key component in semiconductor devices, such as diodes, solar cells and LEDs, can be formed by the close contact of n-type doped silicon and p-type doped silicon [5]. Vapour–liquid–solid (VLS) mechanism [6] is one of the most widely used methods to synthesise silicon nanowires (SiNWs). Typically, SiNWs are synthesised by introducing the volatile silane (SiH₄) gas into the Si/Au nanocluster wafer, in which Au nanoclusters serve as catalysts [7], and the growth direction of SiNWs is usually along [111] direction [6,7]. Recent advances in nanotechnology have enabled to design hybrid materials through combination of nanoscale metal and semiconductor building blocks. Such hybrid metal/silicon materials have much wider applications due to additional functionalities. On the experimental side, Khajepour *et al.* synthesised a gold-on-porous silicon hybrid material with highly sensitive surface-enhanced Raman spectroscopy (SERS) response [8]. Fan *et al.* synthesised a hybrid gold/silicon nanowire photodetector with strong and tunable optical responses [9]. Su *et al.* synthesised gold nanoparticle-decorated SiNWs with strong optical absorbance in the near-infrared (NIR) spectral window, which could be used as NIR hyperthermia agents for cancer photothermal therapy [10].

On the other hand, there have been numerous theoretical studies on the electronic structure, doping and phonon modes of Si nanostructures [11,12]. Computational modelling of metal nanostructures is also reported. Specifically, Meng *et al.* reported the hydrogen dissociation from a charged Pt cluster modelled by *ab initio* molecular dynamics [13]. Neukirch *et al.* reported the first time-domain *ab initio* study of relaxation of plasmon excitation through the phonon channel in a silver quantum dot (QD) [14]. However, few theoretical studies have been performed on hybrid metal nanoparticle/silicon nanostructures, especially on the simulation of phonon-induced relaxation of photo-excited electrons and holes in these hybrid metal nanoparticle/silicon nanostructures.

We have reported theoretical calculations of the optical properties of different types of silicon nanostructures ranging from crystalline to amorphous silicon nanostructures [15]. Here, we present the theoretical studies on the optical and electronic properties of periodic array of Au/Si nanostructure along [111], in which aluminium and phosphorus co-doped silicon QD is inserted into gold nanoclusters. The density functional theory (DFT) is used to compute the electronic structure of the simulated system. Non-adiabatic coupling implemented in the form of dissipative equation of motion for reduced density matrix is used to study the phonon-induced relaxation in the simulated system. The combination of Redfield theory with on-the-fly coupling of electron-to-lattice by the molecular dynamics trajectory based on DFT provides a better tool to study the electronic relaxation [16]. The density of states (DOS) clearly shows that the formation of Au–Si bonds contributes states to the

*Corresponding author. Email: dmitri.kilin@usd.edu

band gap of the model. In addition, simulated results show that for selected photo-excitations, the electron is promoted from aluminium to phosphorus in the photon-mediated process and then recombines to the ground state through golden bridge. In addition, it is observed that the hole relaxation is faster than electron relaxation. The spatial arrangement of periodic array of Au/Si nanostructure prompts that this set up does model the short circuit current.

2. Methods

The electronic structure is determined by using DFT [17] implemented in the Vienna ab initio simulation package (VASP) [18]. Kohn–Sham (KS) equations are employed to self-consistent DFT functions to obtain better approximation. The main equation is a fictitious one-electron KS [19] equation:

$$\left(-\frac{\hbar^2}{2m} \nabla^2 + v \left[\left\{ \vec{R}_I \right\}, \vec{r}, \rho(\vec{r}) \right] \right) \varphi_i^{\text{KS}} \left(\left\{ \vec{R}_I \right\}, \vec{r} \right) = \varepsilon_i \left(\left\{ \vec{R}_I \right\} \right) \varphi_i^{\text{KS}} \left(\left\{ \vec{R}_I \right\}, \vec{r} \right), \quad (1)$$

where the first term corresponds to kinetic energy T and uses symbol of gradient $\nabla = \left(\frac{\partial}{\partial x}, \frac{\partial}{\partial y}, \frac{\partial}{\partial z} \right)$. In Equation (1) we find set of one-electron orbital's $\varphi_i^{\text{KS}}(r)$ and their energies ε_i . The orbitals are combined with orbital occupation function f_i for constructing the total density of electrons as

$$\rho(\vec{r}) = \sum_i f_i \varphi_i^{\text{KS}*}(\vec{r}) \varphi_i^{\text{KS}}(\vec{r}). \quad (2)$$

The total density determines the potential as

$$v[\vec{r}, \rho] = \frac{\delta(E^{\text{tot}}[\rho] - T[\rho])}{\delta\rho}, \quad (3)$$

which is defined as functional derivative of the total energy in respect to variation of the total density and includes interactions of electrons with ions, and three electron interactions: Coulomb, correlation and exchange. Rectangular brackets symbolise functional. Equations (1)–(3) are solved in the iterative, self-consistent manner by using VASP software according to Perdew–Burke–Ernzerhof (PBE) [20,21] form of the generalised gradient approximation (GGA) [20] with the projected augmented wave (PAW) formalism [22].

DOS, absorption spectrum, band energy, molecular dynamic fluctuation and non-adiabatic coupling can be extracted from VASP calculations. The DOS for all orbitals $n(\varepsilon)$ for occupied orbitals $n'(\varepsilon)$ can be expressed as

$$n(\varepsilon) = \sum_i \delta(\varepsilon - \varepsilon_i), \quad (4a)$$

$$n'(\varepsilon) = \sum_i f_i \delta(\varepsilon - \varepsilon_i), \quad (4b)$$

where ε_i is the KS energy of a given orbital, and the index i corresponds to each orbital calculated by using DFT. Occupied orbitals $n'(\varepsilon)$ are filled with red, while unoccupied orbitals $n(\varepsilon)$ have no fill. Here, $f_i \leq \frac{1}{2}$, $i \leq \text{HOMO}$ for the valence band, while $f_i \geq \frac{1}{2}$, $i \geq \text{LUMO}$ for the conduction band (CB). The band gap is defined as band gap = $|\varepsilon_{\text{LUMO}} - \varepsilon_{\text{HOMO}}|$. In Equation (4), $\delta(\varepsilon - \varepsilon_i)$ is the Dirac delta function, modelled by a Lorentzian function:

$$\delta(x) = \frac{1}{\pi} \frac{\sigma}{\sigma^2 + x^2}, \quad (5)$$

where σ is a parameter with the same dimensions as the argument of the delta function which gives the width of the distribution. The value $\sigma = 0.05$ eV was used to simulate spectral line broadening in an experimental measure of the DOS. The absorption spectrum can be expressed as

$$a(\varepsilon) = \sum_{ij} f_{ij} \delta(\varepsilon - \Delta\varepsilon_{ij}), \quad (6)$$

where f_{ij} is the oscillator strength which describes the transition probability from the initial state i to the final state j , and is defined as

$$f_{ij} = \left| \vec{D}_{ij} \right|^2 \frac{4\pi m_e v_{ij}}{3\hbar e^2}, \quad (7)$$

where m_e is the mass of an electron, \hbar is Planck's reduced constant, v_{ij} is resonant frequency and e is the charge of the electron. \vec{D}_{ij} is the electric dipole moment matrix element for the transition between the initial state i and the final j state. \vec{D}_{ij} can be expressed as

$$\vec{D}_{ij} = e \int \varphi_i^{\text{KS}*} \vec{r} \varphi_j d\vec{r}. \quad (8)$$

Electronic structure of atomic models was explored at equilibrium-optimised geometry and along nuclear trajectory $\{\vec{R}_I(t)\}$ modelling system interfacing a thermostat. Positions of ions enter DFT equations as parameters as in Equation (1).

Electronic dissipative transitions $\left(\frac{d\rho_{jk}}{dt} \right)_{\text{diss}}$ are computed along molecular dynamics trajectory for positions of ions $\{\vec{R}_I(t)\}$ with initial conditions for positions $\{\vec{R}_I(t=0)\}$ and velocities $\left\{ \frac{d}{dt} \vec{R}_I(t=0) \right\}$ representing ambient temperature. On-the-fly non-adiabatic couplings are computed along nuclear trajectory as

$$V_{ij}(t) = \frac{-i\hbar}{\Delta t} \int d\vec{r} \varphi_i^{\text{KS}*} \left(\left\{ \vec{R}_I(t) \right\}, \vec{r} \right) \varphi_j^{\text{KS}} \times \left(\left\{ \vec{R}_I(t + \Delta t) \right\}, \vec{r} \right) + \text{h.c.} \quad (9a)$$

An autocorrelation function of the coupling is maximal at $t = 0$ and decays rapidly thereafter

$$M_{ijkl}(\tau) = \frac{1}{T} \int_0^T dt V_{ij}(t + \tau) V_{kl}(t). \quad (9b)$$

A Fourier transform of coupling autocorrelation function [23] provides partial components Γ^\pm

$$\Gamma_{ljik}^+ = \int d\tau M_{ljik}(\tau) \exp(-i\omega_{ik}\tau), \quad (9c)$$

$$\Gamma_{ljik}^- = \int d\tau M_{ljik}(\tau) \exp(-i\omega_{lj}\tau). \quad (9d)$$

These partial components add together and compose Redfield tensor, which controls dynamics of density matrix:

$$R_{ijkl} = \Gamma_{ljik}^+ + \Gamma_{ljik}^- - \delta_{jl} \sum_m \Gamma_{immk}^+ - \delta_{ik} \sum_m \Gamma_{jmml}^-, \quad (9e)$$

$$\left(\frac{d\rho_{jk}}{dt} \right)_{\text{diss}} = \sum_{lm} R_{jklm} \rho_{lm}. \quad (10)$$

Specific initial excitations by a photon, $\hbar\Omega_{AB} = \varepsilon_B - \varepsilon_A$, occur between orbitals A and B. This excitation is described by density matrix at time $t = 0$

$$\rho_{ij}(0) = \delta_{ij}(f_i - \delta_{iA} + \delta_{jB}). \quad (11a)$$

Time evolution of electronic state is calculated by solving the equation of motion as follows:

$$\dot{\rho}_{ij} = -\frac{i}{\hbar} \sum_k (F_{ik}\rho_{kj} - \rho_{jk}F_{ki}) + \left(\frac{d\rho_{ij}}{dt} \right)_{\text{diss}}. \quad (11b)$$

Electronic transitions are facilitated by thermal fluctuations of ions. Numerical solution of Equation (11b) provides time-dependent elements of density matrix $\rho_{kj}(t)$. Of special importance are diagonal elements $\rho_{jj}(t)$, which determine time-dependent occupations of KS orbitals. With the above information, charge density distribution, rate of energy dissipation and rate of charge transfer can be calculated. Specifically, the distribution of charge as a function of energy reads

$$n''(\varepsilon, t) = \sum_i \rho_{ii}(t) \delta(\varepsilon - \varepsilon_i). \quad (11c)$$

The difference of above and equilibrium distribution (see Equation (4b)) provides comprehensive explanation of electron and hole dynamics. The change of the population with respect to the equilibrium distribution is then expressed as

$$\Delta n(\varepsilon, t) = n''(\varepsilon, t) - n'(\varepsilon). \quad (11d)$$

This equation describes a population gain when $\delta n > 0$ and a loss when $\delta n < 0$ at energy ε , which corresponds to the electron and the hole parts of an excitation. Finally, the time evolution of the population of the lowest unoccupied molecular orbital (LUMO) as well as the highest occupied molecular orbital (HOMO) can be fitted to the following equation:

$$P_{e(h)}(t) = 1 - \exp\left(-\frac{t}{\tau^{e(h)}}\right), \quad (12)$$

where e and h refer to the electron in the CB and the hole in the valence band, respectively. The constant $\tau^{e(h)}$ represents the average relaxation time for the electron (hole), and thus the dynamics of the electronic relaxation. Below, we use index e with understanding that equations for holes are the same for electrons. Expectation value of energy of a carrier (electron or hole):

$$\langle \Delta \varepsilon_e \rangle(t) = \sum_i \rho_{ii}(t) \varepsilon_i(t). \quad (13)$$

The above formula can be rewritten to dimensionless energy:

$$\langle E_e \rangle(t) = \frac{\langle \Delta \varepsilon_e \rangle(t) - \langle \Delta \varepsilon_e \rangle(\infty)}{\langle \Delta \varepsilon_e \rangle(0) - \langle \Delta \varepsilon_e \rangle(\infty)}. \quad (14)$$

Assuming single exponential fit of the energy dissipation,

$$\langle E_e \rangle(t) = \exp\{-k_e t\}. \quad (15)$$

Energy dissipation rate can be expressed as follows:

$$k_e = \{\tau^e\}^{-1} = \left\{ \int_0^\infty \langle E_e \rangle(t) dt \right\}^{-1}. \quad (16)$$

3. Results and discussion

Figure 1 shows the optimised geometry of the simulated systems. Each model is optimised in VASP software with DFT by using periodic boundary conditions (PBC). Panel (a) shows the optimised geometry of periodic array of Au/Si nanostructure with a repeating unit (-Au₁₉-Si₃₆Al₁P₁H₃₆-Au₁₉-). To reduce computational expense, we started with a minimalistic model. In the original model, we place doping in any available location away from surface. Replacing inner, four-coordinated silicon atom with either Al or P seems to be more common in experiment. Since the model is very small, any other arrangements would place at least one doping ion at the surface. Surface dopings may contribute additional mechanisms of relaxation and act as a kind of inorganic atomic ligands for Si quantum dots [24] overcoming the bulk Si band gap limitation [25]. Increase

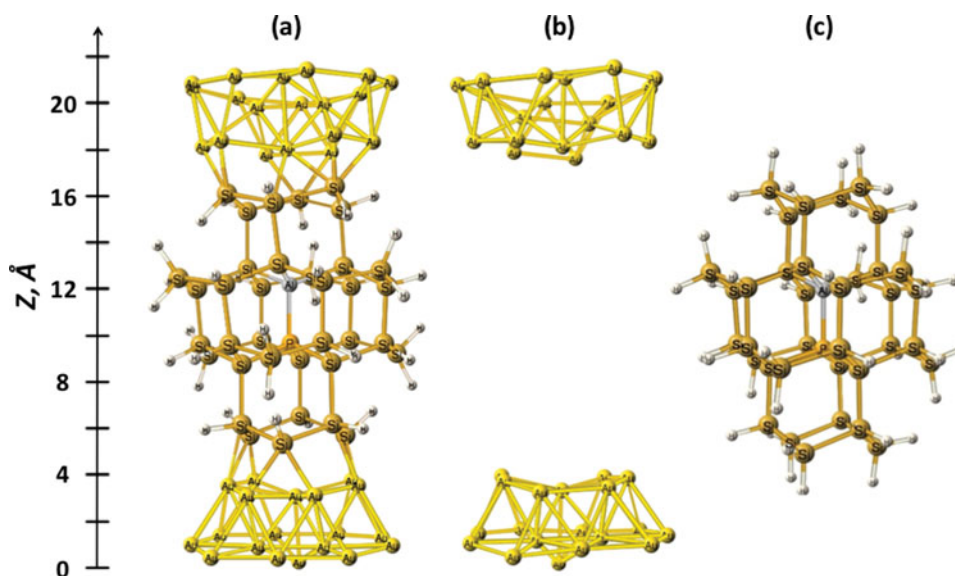


Figure 1. Optimised geometry of three different simulated systems: (a) periodic array of Au/Si nanostructure spreads along [111] direction, (b) Au_{38} cluster and (c) Al and P co-doped Si QD. Vertical z-axis is used to identify space regions filled by different materials. Yellow, dark yellow, orange, white and grey spheres represent Au, Si, P, H and Al, respectively. All models are enclosed in PBC boxes.

in distance between co-dopants affects formation energy and increases radiative lifetime [12,26]. There are two fragments in the atomic model of the periodic array of Au/Si nanostructure. The first one includes Al and P co-doped silicon QD with a formula of $\text{Si}_{36}\text{Al}_1\text{P}_1\text{H}_{36}$. As shown in Figure 1(a), there are four atomic layers of silicon. In the original model, dopants are placed into two middle layers of silicon and are in close proximity to each other. Alternative placements of doping are discussed in SI. The second architecture is the 38-atom gold cluster, which linked to the Si QD. The shape of the Si QD is elliptical, while the shape of the gold cluster is roughly spherical. The Si QD is elongated in [111] direction, and both dopants and gold cluster spread along this direction. Such geometry is of great interest since it mimicks a possible experimental situation. Specifically, VLS method can provide fabrication of Si NWs extended in the [111] crystallographic direction. Our simulation could be a model to determine the impact of the gold contacts in this method. The optimised geometry is characterised by interatomic distances and distribution of interatomic distances, as illustrated in Figure S2 (available as supplemental data in the online version). At the interface, the Au–Si distances have the average value of 2.4868 Å, which is close to the value of 2.47 Å, reported in the literature [27]. These distances can be interpreted as covalent bond formation. According to Figure S2 (available as supplemental data in the online version), such distances are seen in periodic array of Au/Si nanostructure and are absent in the Au_{38} and Al and P co-doped Si QD models.

We also explore the total energy for several placements of dopants into different atomic layers of silicon. The ex-

plored configurations are labelled according to the presence of doping at each of four atomic layers of silicon. Each model is labelled by four symbols. For example, the model, in which both Al and P are placed into the middle layers of silicon but are not in direct contact, is labelled as –Si–Al–P–Si–. All explored models are shown as inserts in Figure S1 (available as supplemental data in the online version). According to Table S1 (available as supplemental data in the online version), one can see the following trend in the total energy:

$$\begin{aligned}
 E_{\text{tot}}(-\text{Al} - \text{Si} - \text{Si} - \text{P}-) &< E_{\text{tot}}(-\text{Al} - \text{Si} - \text{P} - \text{Si}-) \\
 &< E_{\text{tot}}(\text{original}) < E_{\text{tot}}(-\text{Si} - \text{Al} - \text{Si} - \text{P}-) \\
 &< E_{\text{tot}}(-\text{Si} - \text{Al} - \text{P} - \text{Si}-).
 \end{aligned}
 \quad (17)$$

The total energy depends on both factors: proximity of dopants to each other and proximity of dopants to Au. Interestingly, in a configuration where co-dopants are not in direct contact and do not interface gold (–Si–Al–P–Si–), the total energy is the least preferred. The DOS and partial density of states (PDOS) of such models with different positions of dopants can be found in Figure S1 (available as supplemental data in the online version).

Panels (b) and (c) in Figure 1 show the optimised geometry of Au_{38} cluster and Al and P co-doped Si QD with a formula of $\text{Si}_{36}\text{Al}_1\text{P}_1\text{H}_{42}$, respectively. The Au_{38} cluster is derived from the periodic array of Au/Si nanostructure by deliberately omitting other atoms without changing the orientation of Au atoms and the size of the supercell. The

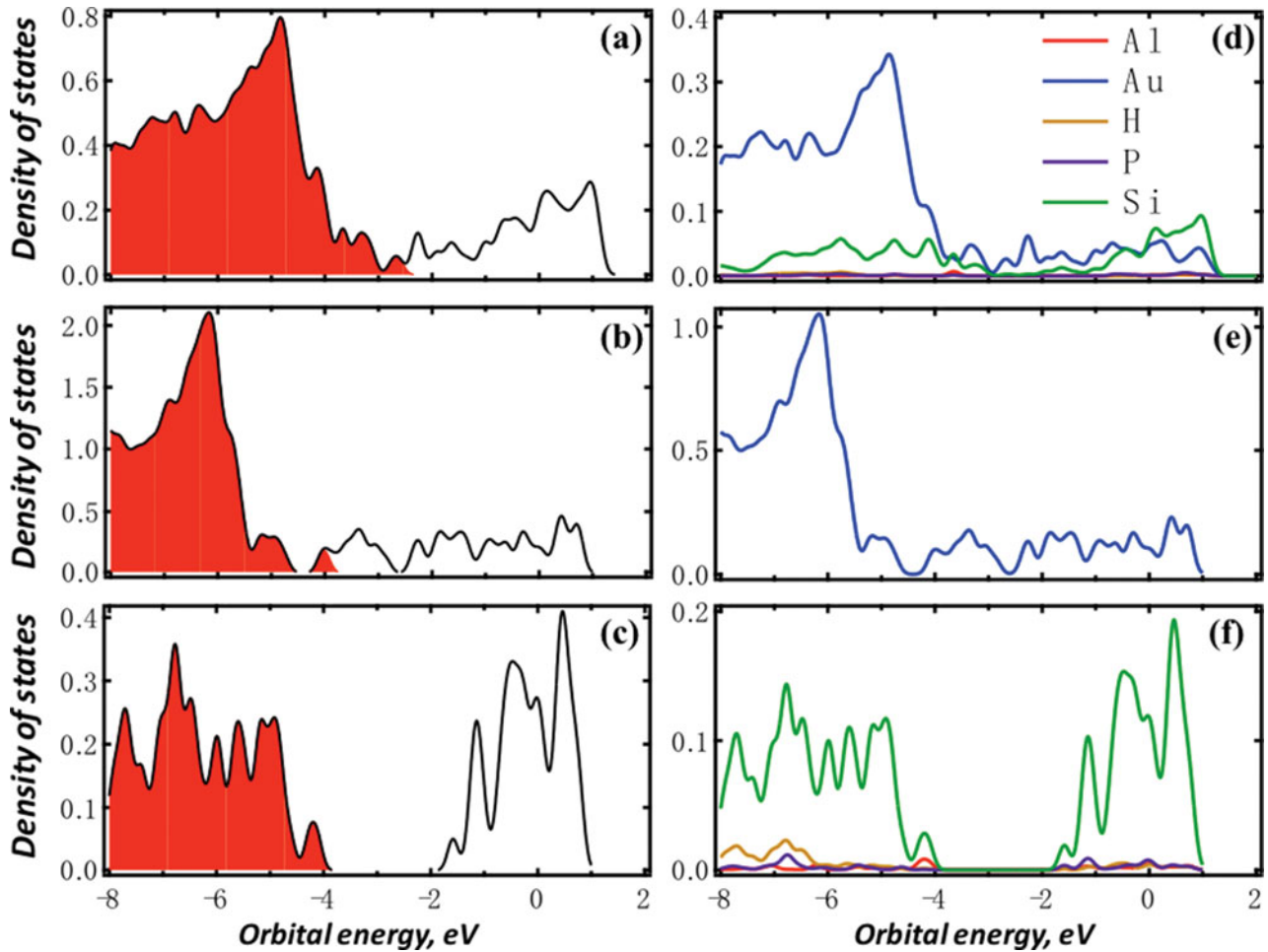


Figure 2. Density of states and partial density of states of three different systems at 0 K. Panels (a) DOS and (d) PDOS of periodic array of Au/Si nanostructure; panels (b) DOS and (e) PDOS of Au₃₈ cluster; and panels (c) DOS and (f) PDOS of Al and P co-doped Si QD. Energy gap $E_g(\text{Au-Si}) = 0.2810$ eV, $E_g(\text{Au}) = 0.1515$ eV and $E_g(\text{Si}) = 2.5395$ eV. Red, blue, orange, purple and green represent Al, Au, H, P and Si, respectively, for panels (d)–(f).

structure of co-doped Si QD is the same as previously reported [28].

Figure 2 shows DOS and PDOS of three different systems. It shows clearly that DOS of periodic array of Au/Si nanostructure has some features of DOS of both Au₃₈ cluster and Al and P co-doped Si QD. The features of silicon part are modified. In addition, new features are introduced, owing to the fact that electronic states are largely affected by incorporating gold atoms into vicinity of Al and P co-doped Si QD. It could be noted that the DOS of periodic array of Au/Si nanostructure and Au₃₈ cluster show vanishing band gap, since some of the gold orbitals are supposed to be surface states [29]. On the basis of PDOS of periodic array of Au/Si nanostructure, it can be concluded that the states in valence band (VB) are mainly attributed to Au, while the states in CB are mainly attributed to both Au and Si. The contribution of dopant near band gap is not obvious. However, PDOS of Al and P co-doped Si QD reveals that the contribution of dopants to the states near band gap is clear.

Such observation further proves the influence of formation of hybrid silicon–gold orbitals. DOS of periodic array of Au/Si nanostructure cannot be obtained by a superposition of DOS of Au₃₈ cluster and DOS of Al and P co-doped Si QD. Thus, it is reasonable to assume that electronic structure of periodic array of Au/Si nanostructure is affected by an interaction of Si and Au parts and has two types of contributions: (i) specific states contributed by compensation of dangling bonds and formation of chemical bonds at Au–Si interface and (ii) mutual shift of energies of Si bands by Au and Au bands by Si, related to band bending at Au–Si interface.

Figure 3 shows absorption spectra of three different simulated systems at 0 K. It shows that in the range from 0 to 2.8 eV, the absorption spectrum of periodic array of Au/Si nanostructure is similar to that of Au₃₈ cluster, as can be seen from peaks g, f of panel (a) and peaks g', f' of panel (b). In the same range, no absorption is observed for Al and P co-doped Si QD, indicating that the main contributor

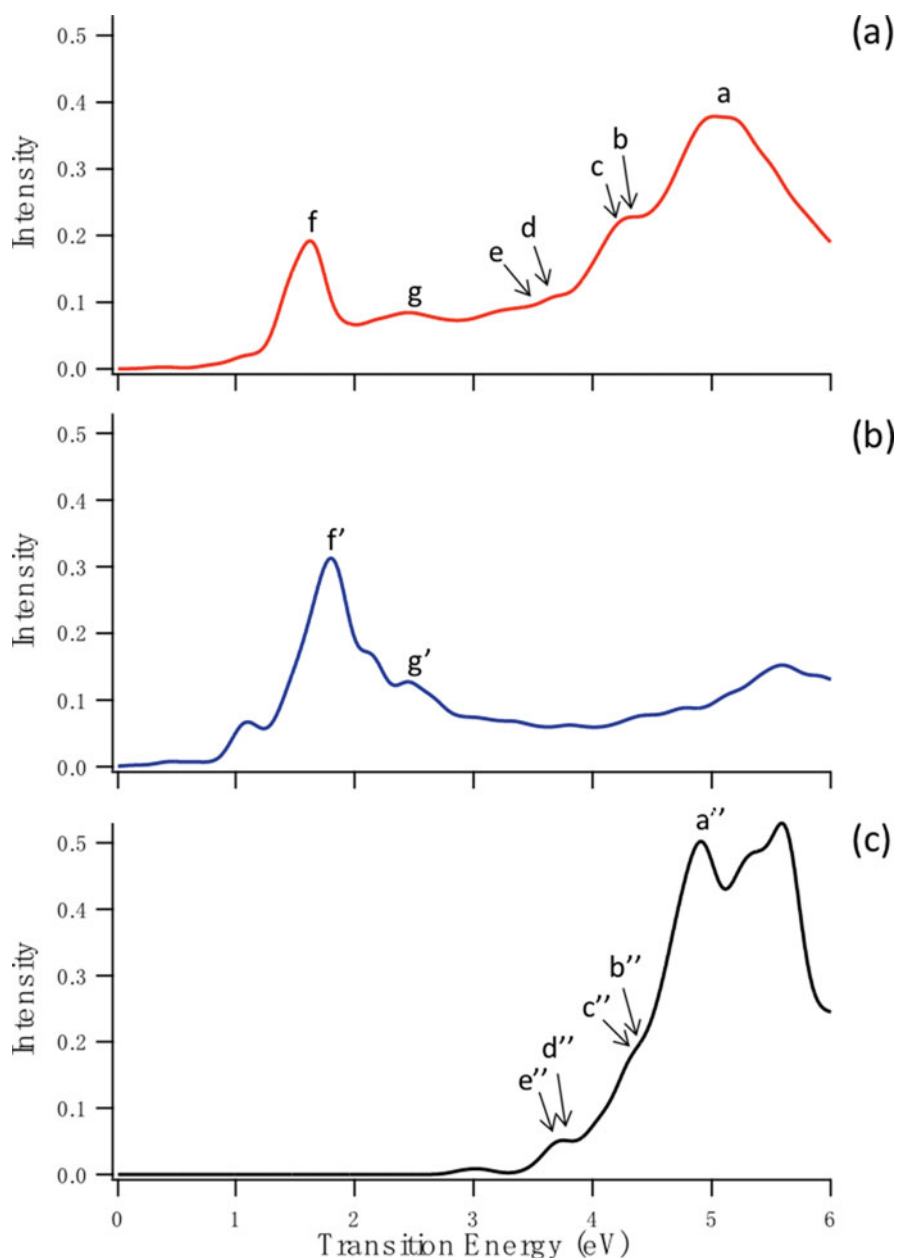


Figure 3. Absorption spectra of three different systems at 0 K. Panel (a) periodic array of Au/Si nanostructure with the most probable optical transitions labelled. Panel (b) Au₃₈ cluster and panel (c) Al and P co-doped Si QD. Absorption features a–f of the Au/Si nanostructure are similar to absorption features g’–f’ of Au nanostructure and a’’–e’’ of Si nanostructure.

is gold cluster. However, the small peaks around 1.1 and 2.1 eV are only observed in the spectrum of Au₃₈ cluster. The peak shift and absence of small peaks in the spectrum of periodic array of Au/Si nanostructure might be due to contribution of dangling bonds between Si and Au atoms. In the range from 2.8 to 6.0 eV, the absorption spectrum of periodic array of Au/Si nanostructure is similar to that of Al and P co-doped Si QD, and the absorbance of gold cluster is relatively low, indicating that silicon is the main contributor in this range. Interestingly, only one broad absorption peak

(peak *a* around 5.2 eV) presents in the spectrum of periodic array of Au/Si nanostructure, while two peaks (around 4.8 and 5.6 eV) are observed in the spectrum of Al and P co-doped Si QD. Such changes are probably due to the formation of Au–Si bonds.

Figure 4 shows the fluctuation of the vibrational energy of KS orbital $\varepsilon_i(t)$ from HO-20 to LU + 20 along molecular dynamics trajectory for periodic array of Au/Si nanostructure. Each colourful line represents a distinct KS orbital. E_{Fermi} , which is labelled by the black dashed line,

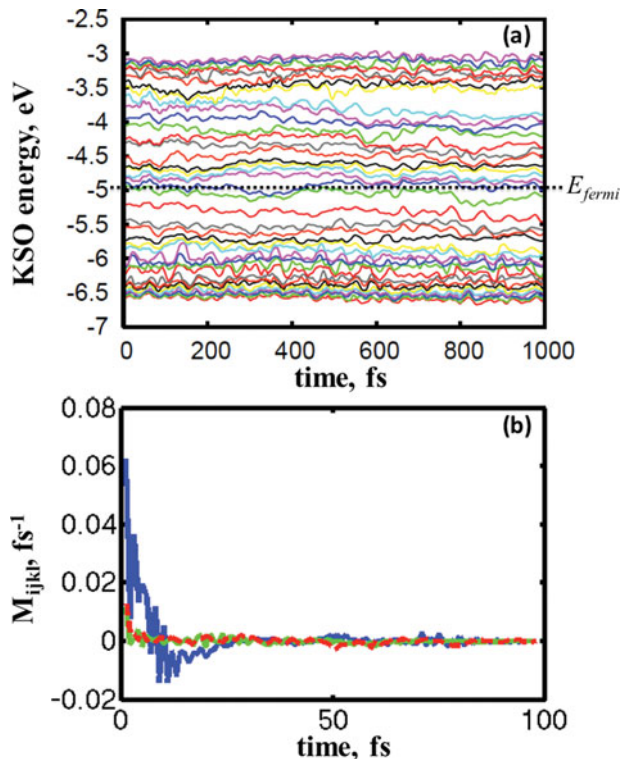


Figure 4. Panel (a) fluctuation of KS orbital energy $\varepsilon_i(t)$ as a function of time for periodic array of Au/Si nanostructure. E_{Fermi} is labelled as the black dashed line. These results are acquired from *ab initio* molecular dynamics simulations at 300 K over 1000 fs. Panel (b) examples of autocorrelation functions for non-adiabatic coupling matrix elements, according to Equation 9(b). Shown are autocorrelation functions $M_{ijkl}(\tau)$ for $i = k$ and $j = l$, for the following pairs of orbitals: $i = \text{HO-2}, j = \text{HO-1}$ (green), $i = \text{HO}, j = \text{LU}$ (blue), $i = \text{LU}, j = \text{LU} + 1$ (red). Interestingly, all of them decay abruptly within 5 fs.

is found at -4.9338 eV. Figure 4(a) is consistent with Figure 2 by adding the value of $\alpha + \beta$ to obtain the absolute eigenvalues (i.e. corrected $E_{\text{Fermi}} = E_{\text{Fermi}} + \alpha + \beta = -2.5023 - 2.4315 = -4.9338$ eV). In Figure 2, the DOS is very large at energies $E < -4.0$ eV, which is about 1.5 eV below the E_{Fermi} . In Figure 4(a), the orbital energies are very close to each other at energies $E <$

-6.4 eV, which is also about 1.5 eV below E_{Fermi} . In addition, it should be noted that no distinction between HO and LU can be found in Figure 4(a), since the energy gap between HO and LU is small (about 0.2810 eV). Details about the molecular dynamics of periodic array of Au/Si nanostructure can be found in [30].

Figure 4(b) illustrates several examples of $M_{ijkl}(\tau)$ – the autocorrelation function of electron-to-lattice non-adiabatic interaction computed according to Equation (9b). Amplitude of these functions provides an intensity of dissipative electronic transitions for given indices i, j, k, l . Interestingly, for any tested combination of indices the autocorrelation function decays abruptly within less than 5 fs. This observation justifies Markovian approximation and time-independent form of relaxation kernel in Equations (9e)–(10).

Results of electron and hole dynamics of periodic array of Au/Si nanostructure upon photo-excitation energy about 4.2286 eV corresponding to feature *c* of Figure 3(a) are presented in Figure 5. Panel (a) shows distribution of charge as a function of energy and time. It is noted that there are multiple intermediate states during electron relaxation, while few or no intermediate states are observed during the hole relaxation. It is observed from panel (a) that hole relaxation is much faster than electron relaxation. Hole relaxation completes after 0.7 ps, while electron relaxation completes after 4.3 ps, as recorded in Table 1. This result is consistent with the computed DOS of periodic array of Au/Si nanostructure, in which the DOS for VB is much higher than that of the CB. The higher DOS is responsible for the smaller energy gap between electronic states and provides more relaxation channels. Figure 5 shows that upon initial photo-excitation, electron resides in LU + 44 and hole resides in HO-8, at $t \approx 5$ fs. At $t \approx 300$ fs, the electron and hole relax to the intermediate states LU + 42 and HO-5, respectively. At the final stage $t \approx 20$ ps, the electron occupies LU and the hole occupies HO. Panel (b) provides details on electron dynamics in space. It shows that electrons transfer from Al to P, and finally relax to Au. Panel (c) shows hole dynamics in space. It shows that hole dynamics for $100 \text{ fs} < t < 1 \text{ ps}$ have same average energy but different spatial localisation. This result is due

Table 1. Non-adiabatic dynamics computation of energy dissipation rates k_e , k_h and k_{ex} for different excitations, according to Eq. 16.

Label in Fig. 3	Hole orbital, i	Electron orbital, j	iH = HO- i +1	iE = j -HO	Oscillator strength	Transition energy	k_e, ps^{-1}	k_h, ps^{-1}	$k_{\text{ex}} = k_e + K_h, \text{ps}^{-1}$
a	267	346	37	43	0.833757	5.0456	0.2260	1.6290	1.8550
b	295	349	9	46	0.996108	4.2452	0.2238	1.3876	1.6114
c	295	348	9	45	0.029416	4.2286	0.2302	1.3876	1.6178
d	284	327	20	24	0.564501	3.7529	0.1879	1.8862	2.0741
e	300	345	4	42	0.423519	3.6294	0.2270	1.2613	1.4883
f	302	330	2	27	1.129521	2.5494	0.1938	1.6389	1.8327
g	298	310	6	7	5.204847	1.6108	0.2346	1.1532	1.3878

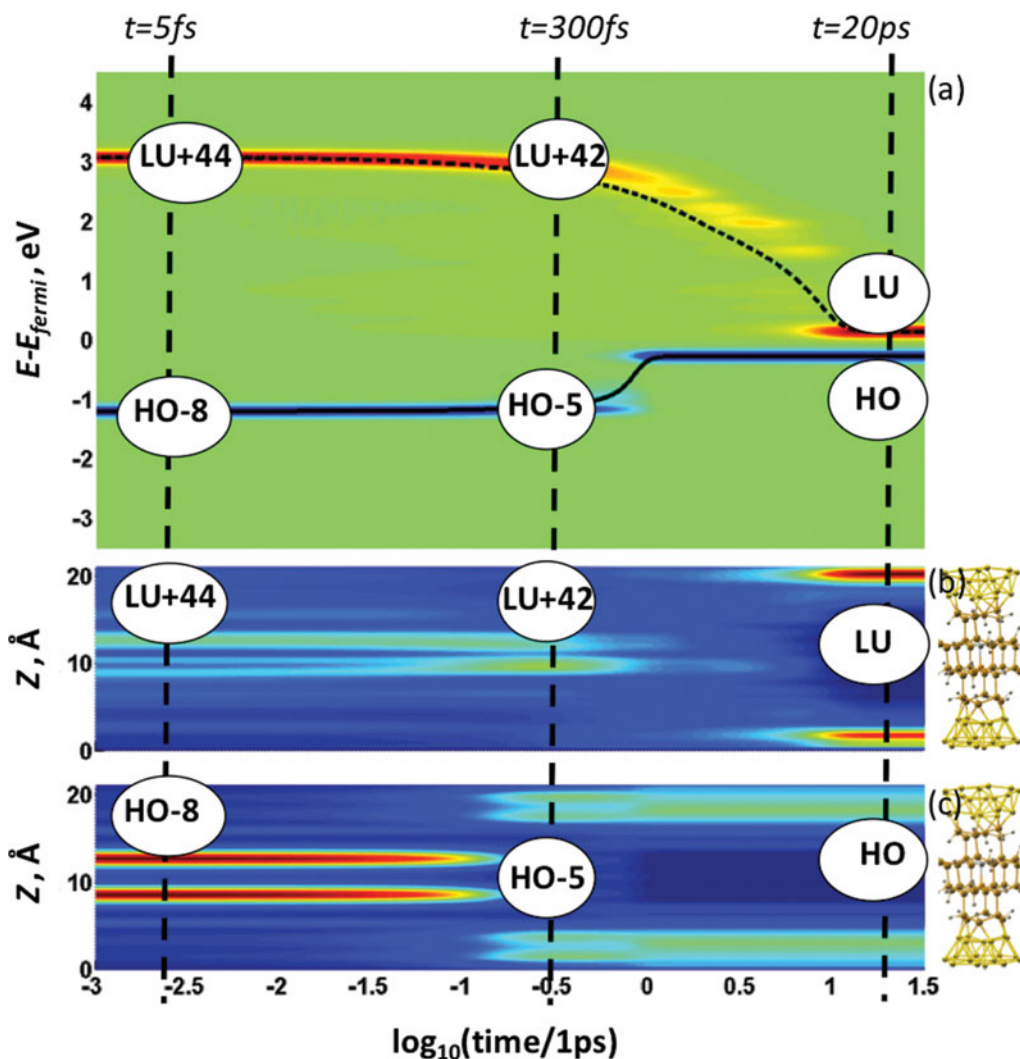


Figure 5. Representative relaxation dynamics of periodic array of Au/Si nanostructure upon photo-excitation energy about 4.2286 eV. Panel (a) shows distribution of charge as a function of energy and time, with colour code red, green, blue representing electron, equilibrium distribution, and hole. Dashed and solid lines indicate expectation values for energy, calculated in an energy space distribution for conduction and valence bands, respectively. Panel (b) provides details on electron dynamics in space. Panel (c) shows hole dynamics in space. The range of time is the same for all three panels.

to several occupied orbitals of Si and Au which are very close in energy. Electron and hole dynamics in space also confirm that hole relaxation is much faster than electron relaxation and both hole and electron finally relax to the gold cluster. Actually, it is found that for HO about 86% of the charge is localised on Au, and for LU about 96% of the charge is localised on Au.

Pairs of occupied and unoccupied KS orbitals participating in the electron and hole dynamics induced by low-energy optical transitions at 4.2286 eV excitation for the atomic model of periodic array of Au/Si nanostructure are visualised in Figure 6. Interestingly, panel (g) in Figure 6 illustrates HOMO having non-zero charge density in space between Au and Si atoms. The bonding character of HOMO is an indirect indication of Au–Si chemical bond formation.

The reaction of hole transfer to gold can be expressed in Equation (18a), and is quicker than the reaction of electron transfer to gold in Equation (18b):



It should be noted that actual dynamics is more complicated (see Table 1, non-adiabatic coupling computation of energy dissipation rates k_e , k_h and k_{ex} in different excitation), and the details of role of Al and P doping are discussed in SI.

A possible physical explanation for the charge carrier dynamics is that Au/Si interface is polarised. Silicon side of interface, in ground state, is enriched with positive charge

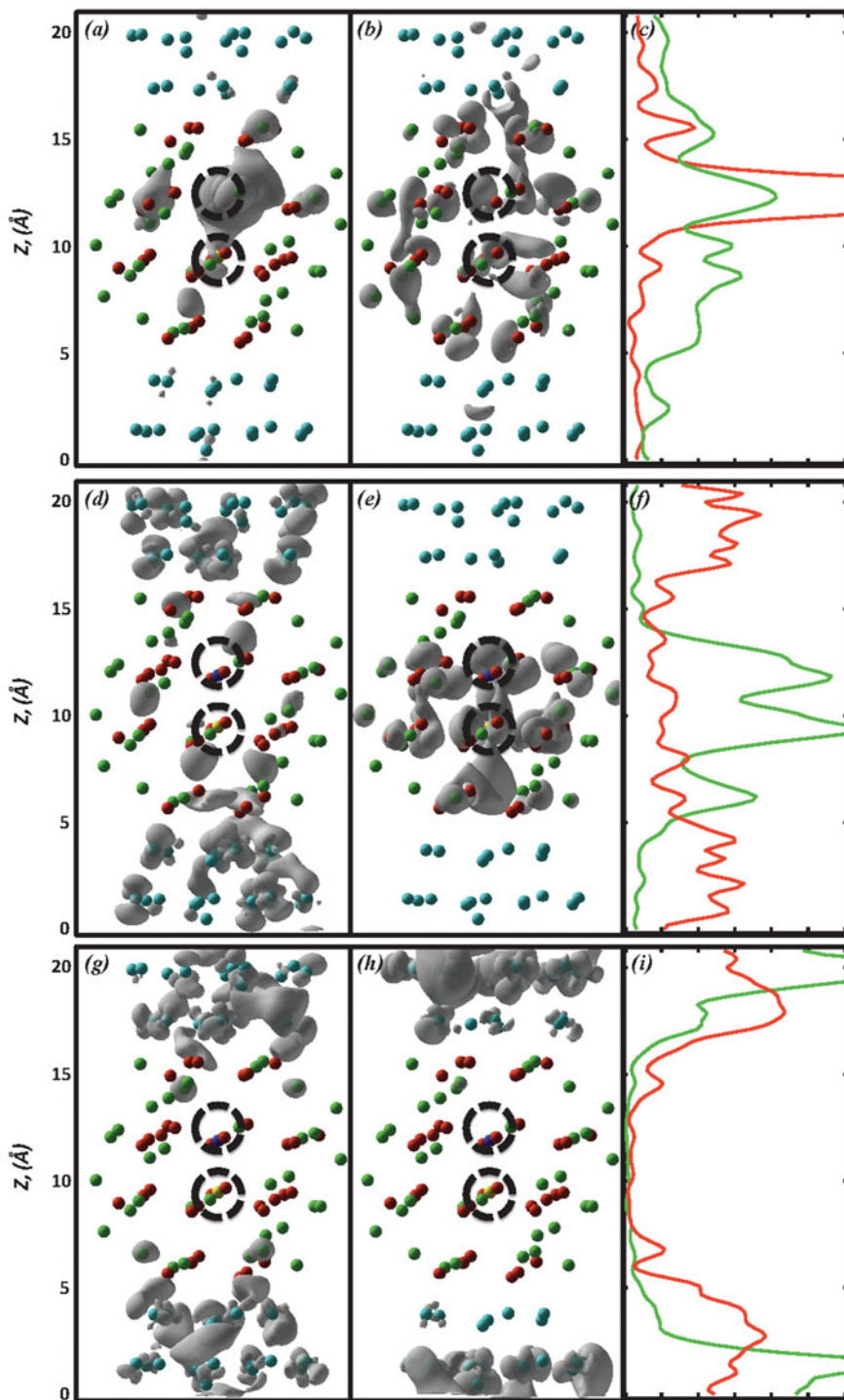


Figure 6. Pairs of occupied and unoccupied KSOs contributing to low-energy optical transitions, for the atomic model of periodic array of Au/Si nanostructure. Red, green, blue, yellow and dark blue stand for Si, H, Au, P and Al, respectively. Black dashed circles pointing at Al and P atoms. Grey clouds represent isosurfaces of KSO. Panels (a), (b), (d), (e), (g) and (h) show partial charge density of a given KSO. Panels (c), (f) and (i) show partial charge density integrated over the x, y direction, as a function of z ; The transition HO-8 to LU + 44 at transition energy 4.2286 eV is represented by panels (a)–(c) and corresponds to label *c* in Table 1. Panel (a) shows partial charge density of HO-8. Panel (b) shows partial charge density of LU + 44. Red and green in panel (c) represents 1D projection of orbital HO-8 and LU + 44 on z -direction, respectively. The transition HO-5 to LU + 42 is represented by panels (d)–(f). Panels (d) and (e) show partial charge density of HO-5 and LU + 42 orbitals, respectively. Panel (f) represents projections of orbitals on z -direction. Red and green in panel (f) stand for HO-5 and LU + 42 orbitals, respectively. The transition HO to LU is represented by panels (g)–(i). Panels (g) and (h) show partial charge density of HO and LU orbitals, respectively. Panel (i) represents projections of orbitals on z -direction. Red and green in panel (i) stand for HO and LU orbitals, respectively.

that favours electron transfer from Au to Si and disfavours electron transfer from Si to Au. A possible quantum chemical explanation is that DOS of VB of Au is higher than DOS of CB of Au. The last statement is supported by numerical data as follows. The numerical values of DOS at different energies, defined in Equation (4a), are evaluated at energies $E_{VB} < E_{CB}$ and are found to follow a specific inequality, $n(E_{VB}) > n(E_{CB})$. Here, E_{VB} corresponds to energy near and below Fermi energy of the Au part of the material. $E_{VB} < E_{Fermi}$. E_{CB} corresponds to energy near and above Fermi energy of the Au part of the material. $E_{CB} > E_{Fermi}$. Energies enter as arguments in the inequality for DOS values.

4. Conclusion

In summary, we have presented theoretical studies of minimalistic model of periodic array of Au/Si nanostructure. Results of DOS of periodic array of Au/Si nanostructure, Au₃₈ cluster, and Al and P co-doped Si QD indicate that additional states will be introduced due to gold contacts. The absorption spectra show that periodic array of Au/Si nanostructure has features contributed by both Al and P co-doped Si QD and Au₃₈ cluster. Non-adiabatic coupling allows studies of the hole and electron dynamics of periodic array of Au/Si nanostructure and shows what happens after electrons are excited into CB leaving holes in VB upon initial photo-excitation. During the relaxation process, electrons and holes migrate in energy and in space and the electronic excitation is converted into vibrational energy. Moreover, hole relaxation in energy and in space is much faster than electron relaxation, which is due to the higher DOS of the valence band. The microscopic information that holes arrive earlier than electrons to gold electrode is rather important for nanoelectronics. It would be interesting to explore if these calculated properties affect the photoconductivity of such periodic nanostructure [31].

Acknowledgements

We thank the NSF/EPSCoR award EPS0903804, and the State of South Dakota, governor's Office of Economic Development. The computational resources of DOE, BES – Chemical Sciences, NERSC Contract No. DE-AC02-05CH11231, allocation Awards 85213 and 86185 'Computational Modeling of Photo-catalysis and Photoinduced Charge Transfer Dynamics on Surfaces' are gratefully acknowledged. Computational resources of USD High Performance Computing facilities cosponsored by South Dakota IDeA Networks of Biomedical Research Excellence NIH 2 P20 RR016479 and maintained by Douglas Jennewein are gratefully acknowledged. Inspiring discussions with Mary T. Berry (USD), P. Stanley May (USD) on photoexcited nanomaterials and with Tom Picraux (LANL) and Sergei Ivanov (Los Alamos National Lab, New Mexico) on doped nanowires are acknowledged. We also acknowledge support of Center for Integrated Nanotechnology (CINT) and Center for Nonlinear Studies (CNLS) at Los Alamos National Laboratory (LANL). LANL is operated by Los Alamos National Security, LLC, for the National Nuclear Security

Administration of the US Department of Energy under contract DE-AC52-06NA25396.

Supplemental data

Supplemental materials Supplemental data for this article can be accessed here.

References

- [1] Y. He, Y.L. Zhong, F. Peng, X.P. Wei, Y.Y. Su, Y.M. Lu, S. Su, W. Gu, L.S. Liao, and S.T. Lee, *J. Am. Chem. Soc.* **133** (36), 14192–14195 (2011); Y. He, Y.Y. Su, X. B. Yang, Z.H. Kang, T.T. Xu, R.Q. Zhang, C.H. Fan, and S.T. Lee, *J. Am. Chem. Soc.* **131** (12), 4434–4438 (2009); Y. He, Z.H. Kang, Q.S. Li, C.H.A. Tsang, C.H. Fan, and S.T. Lee, *Angew. Chem. Int. Ed.* **48** (1), 128–132 (2009); D.D.D. Ma, C.S. Lee, F.C.K. Au, S.Y. Tong, and S.T. Lee, *Science* **299** (5614), 1874–1877 (2003); Z.F. Ding, B.M. Quinn, S.K. Haram, L.E. Pell, B.A. Korgel, and A.J. Bard, *Science* **296** (5571), 1293–1297 (2002); L. Pavesi, L. Dal Negro, C. Mazzoleni, G. Franzo, and F. Priolo, *Nature* **408** (6811), 440–444 (2000); A. Kar, P.C. Upadhyay, S.A. Dayeh, S.T. Picraux, A.J. Taylor, and R.P. Prasankumar, *IEEE J. Sel. Top. Quantum Electron.* **17** (4), 889–895 (2011).
- [2] A.I. Hochbäum and P.D. Yang, *Chem. Rev.* **110** (1), 527–546 (2010).
- [3] G.J. Zhang, G. Zhang, J.H.Y. Chua, R.E. Chee, E.H. Wong, A. Agarwal, K.D. Buddharaju, N. Singh, Z.Q. Gao, and N. Balasubramanian, *Nano Lett.* **8** (4), 1066–1070 (2008); A.A. Talin, L.L. Hunter, F. Leonard, and B. Rokad, *Appl. Phys. Lett.* **89**, 153102 (2006).
- [4] S.A. Fischer and O.V. Prezhdo, *J. Phys. Chem. C* **115** (20), 10006–10011 (2011).
- [5] A. Boukai, P. Haney, A. Katzenmeyer, G.M. Gallatin, A.A. Talin, and P.D. Yang, *Chem. Phys. Lett.* **501** (4–6), 153–158 (2011); J. Yoo, S.A. Dayeh, W. Tang, and S.T. Picraux, *Appl. Phys. Lett.* **102**, 093113 (2013).
- [6] R.S. Wagner and W.C. Ellis, *Appl. Phys. Lett.* **4** (5), 89–90 (1964).
- [7] Y. Cui, L.J. Lauhon, M.S. Gudiksen, J.F. Wang, and C.M. Lieber, *Appl. Phys. Lett.* **78** (15), 2214–2216 (2001).
- [8] K.J. Khajepour, T. Williams, L. Bourgeois, and S. Adeloju, *Chem. Commun.* **48** (43), 5349–5351 (2012).
- [9] P.Y. Fan, U.K. Chettiar, L.Y. Cao, F. Afshinmanesh, N. Enggheta, and M.L. Brongersma, *Nature Photon* **6** (6), 380–385 (2012).
- [10] Y.Y. Su, X.P. Wei, F. Peng, Y.L. Zhong, Y.M. Lu, S. Su, T.T. Xu, S.T. Lee, and Y. He, *Nano Lett.* **12** (4), 1845–1850 (2012).
- [11] D. Kilin, J. Ramirez, and D. Micha, *Abstr. Pap. Am. Chem. Soc.* 241 (2011); M.G. Mavros, D.A. Micha, and D.S. Kilin, *J. Phys. Chem. C* **115** (40), 19529–19537 (2011); D. Kilin and D. Micha, *Chem. Phys. Lett.* **461** (4–6), 266–270 (2008); S. Ögüt, J.R. Chelikowsky, and S.G. Louie, *Phys. Rev. Lett.* **79** (9), 1770–1773 (1997).
- [12] T.L. Chan, M.L. Tiago, E. Kaxiras, and J.R. Chelikowsky, *Nano Lett.* **8** (2), 596–600 (2007).
- [13] Q.G. Meng, P.S. May, M.T. Berry, and D. Kilin, *Int. J. Quantum Chem.* **112** (24), 3896–3903 (2012); Q. Meng, G. Yao and D. Kilin ACS Symposium Series, Vol. **1140**, pp. 173–185 (American Chemical Society, Washington, DC, 2013).
- [14] A.J. Neukirch, Z.Y. Guo, and O.V. Prezhdo, *J. Phys. Chem. C* **116** (28), 15034–15040 (2012).
- [15] D. Arlund, D.A. Micha, and D.S. Kilin, *Int. J. Quantum Chem.* **110** (15), 3086–3094 (2010); T.W. Lajoie, J.J. Ramirez, D.S. Kilin, and D.A. Micha, *Int. J. Quantum Chem.*

- 110** (15), 3005–3014 (2010); J.J. Ramirez, D.S. Kilin, and D.A. Micha, *Int. J. Quantum Chem.* **109** (15), 3694–3704 (2009); J.J. Ramirez, D.S. Kilin, and D.A. Micha, *Int. J. Quantum Chem.* **112** (1), 300–313 (2012); A. Kryjevski, D. Kilin, and S. Kilina *J. Renew. Sust. Energ.* **5**, 043120 (2013).
- [16] W.B. Davis, M.R. Wasielewski, M.A. Ratner, V. Mujica, and A. Nitzan, *J. Phys. Chem. A* **101** (35), 6158–6164 (1997); O. Kuhn, V. May, and M. Schreiber, *J. Chem. Phys.* **101** (12), 10404–10416 (1994); V. Sundström, T. Pullerits, and R. van Grondelle, *J. Phys. Chem. B* **103** (13), 2327–2346 (1999); J.M. Jean, R.A. Friesner, and G.R. Fleming, *J. Chem. Phys.* **96** (8), 5827–5842 (1992); W.T. Pollard, A.K. Felts, and R.A. Friesner, *Adv. Chem. Phys. Vol XCIII* **93**, 77–134 (1996); W.T. Pollard and R.A. Friesner, *J. Chem. Phys.* **100** (7), 5054–5065 (1994); D. Egorova, M. Thoss, W. Domcke, and H.B. Wang, *J. Chem. Phys.* **119** (5), 2761–2773 (2003); A.G. Redfield, *IBM J. Res. Dev.* **1** (1), 19–31 (1957); P.A. Apanasevich, S. Ya Kilin, A.P. Nizovtsev, and N.S. Onishchenko, *J. Opt. Soc. Am. B* **3** (4), 587–594 (1986); D.S. Kilin and D.A. Micha, *J. Phys. Chem. Lett.* **1** (7), 1073–1077 (2010); I.-H. Chu, H.-P. Cheng, and D.S. Kilin *J. Phys. Chem. C* **117** (35), 17909–17918 (2013).
- [17] P. Hohenberg and W. Kohn, *Phys. Rev.* **136** (3B), B864–B871 (1964).
- [18] G. Kresse and J. Furthmüller, *Phys. Rev. B* **54** (16), 11169–11186 (1996); G. Kresse and J. Hafner, *Phys. Rev. B* **49** (20), 14251–14269 (1994); G. Kresse and J. Furthmüller, *Comput. Mat. Sci.* **6** (1), 15–50 (1996); G. Kresse and J. Hafner, *Phys. Rev. B* **47** (1), 558–561 (1993).
- [19] W. Kohn and L.J. Sham, *Phys. Rev.* **140** (4A), A1133–A1138 (1965).
- [20] J.P. Perdew, K. Burke, and M. Ernzerhof, *Phys. Rev. Lett.* **77** (18), 3865–3868 (1996).
- [21] J.P. Perdew, K. Burke, and M. Ernzerhof, *Phys. Rev. Lett.* **78**, 1396 (1997).
- [22] P.E. Blochl, *Phys. Rev. B* **50** (24), 17953–17979 (1994); D. Hobbs, G. Kresse, and J. Hafner *Phys. Rev. B* **62** (17), 11556–11570 (2000).
- [23] T.M. Inerbaev, J.D. Hoefelmeyer, and D.S. Kilin, *J. Phys. Chem. C* **117**, 9673 (2013); S. Jensen and D. Kilin, *ACS Symposium Series*, Vol. **1140**, pp. 187–218 (American Chemical Society, Washington, DC, 2013); Y. Zhang, C. Qiu, and D. Kilin, *Mol. Phys.*, in press, (2013). DOI:10.1080/00268976.2013.836609.
- [24] H. Sugimoto, M. Fujii, K. Imakita, S. Hayashi, and K. Akamatsu, *J. Phys. Chem. C* **117** (13), 6807–6813 (2013).
- [25] H. Sugimoto, M. Fujii, K. Imakita, S. Hayashi, and K. Akamatsu, *J. Phys. Chem. C* **117** (22), 11850–11857 (2013).
- [26] Y.S. Ma, X.B. Chen, X.D. Pi, and D.R. Yang, *J. Nanopart. Res.* **14** (4), 1, 802–807 (2012); Q. Xu, J.W. Luo, S.S. Li, J.B. Xia, J.B. Li, and S.H. Wei, *Phys. Rev. B* **75**, 235304 (2007); F. Iori, E. Degoli, R. Magri, I. Marri, G. Cantele, D. Ninno, F. Trani, O. Pulci, and S. Ossicini, *Phys. Rev. B* **76**, 085302 (2007); H. Peelaers, B. Partoens, and F.M. Peeters, *Nano Lett.* **6** (12), 2781–2784 (2006).
- [27] I.K. Robinson, P.A. Bennett, and F.J. Himpsel, *Phys. Rev. Lett.* **88**, 096104 (2002).
- [28] J.C. Chen, A. Schmitz, and D.S. Kilin, *Int. J. Quantum Chem.* **112** (24), 3879–3888 (2012); J. Chen, A. Schmitz, T. Inerbaev, Q. Meng, S. Kilina, S. Tretiak, and D. Kilin, *J. Phys. Chem. Lett.* **4** (17), 2906–2913 (2013).
- [29] O. Lopez-Acevedo, H. Tsunoyama, T. Tsukuda, H. Häkkinen, and C.M. Aikens, *J. Am. Chem. Soc.* **132** (23), 8210–8218 (2010).
- [30] Y. Han and D. Kilin, Video-sharing website, YOUTUBE, L.L.C. <http://youtu.be/9018NFB9tU> (accessed on September 24, 2013).
- [31] D.S. Kilin, K.L. Tsemekhman, S.V. Kilina, A.V. Balatsky, and O.V. Prezhdo, *J. Phys. Chem. A*, **113** (16), 4549–4556 (2009).